

Optimization of preheating and interpass temperature in WADED magnesium alloy AZ61: A comparative study on microstructure, residual stresses, and internal defects

Jakub Slavíček¹, Stanislav Zeman¹, Miroslava Horynová², Sascha Senck³, Daniel Koutný¹

This study examines the effect of base material preheating in Wire Arc Direct Energy Deposition (WADED) of AZ61 magnesium alloy. First, the influence of preheating on the geometry of single-track weld beads was evaluated. These findings were then used to identify an appropriate preheating temperature for stabilising the layer width in thin-walled structures. Two preheating strategies were tested, showing that preheating the base material to 200 °C with the same interpass temperature provided the best stability and improved the uniformity of individual layers. In the second part, the impact of preheating on residual stress reduction was assessed by analysing the deformation of the base material. Results showed that preheating reduced residual stresses by up to 50% compared with fabrication without preheating. In addition, material characterisation was performed to evaluate the microstructure and clarify the mechanisms of porosity formation, which was revealed by μ CT scanning in the samples. Preheating positively affected wall thickness stabilisation, residual stress reduction, and porosity. Overall, a temperature of 250 °C was assessed as the most suitable preheating and interpass temperature.

Keywords: Magnesium alloy, preheating, interpass temperature, WADED, WAAM, AZ61

Magnesium alloys, exhibiting low density and a high strength-to-weight ratio, are increasingly used in industries where the product's final weight is essential. For example, reducing weight while replacing aluminium and steel automotive parts with magnesium can reach up to 50%¹. Use of such parts in the automotive and aerospace industry allows reduction in fuel consumption and therefore more economical and environmentally-friendly operation of vehicles¹⁻⁴. Furthermore, the excellent heat dissipation performance and electromagnetic and radio frequency shielding properties of Mg alloys make them good candidates for commercial portable 3C products and military electronic devices^{1,5}. Together with its high recyclability, magnesium alloys, as stated in late review articles^{2,3}, are considered the most promising green engineering materials in the 21st century. However, the production of magnesium parts has limitations due to the hexagonal crystal structure and the limited number of easily-activated slip modes. Therefore, magnesium alloys exhibit plastic deformation anisotropy, limiting the use of traditional manufacturing processes based on plastic deformation. Thus, 90% of magnesium-based parts are produced by casting^{6,7}. That is the most economical way to transform magnesium alloys into shaped components. Still, it is also connected with numerous casting defects and production of scrap metal^{6,8,9}.

The above-mentioned limitations of magnesium are the driving force for improvement of conventional techniques and the invention of new manufacturing methods. One of the main research directions suggested in literature¹⁰ is further improvement of advanced processing technologies of Mg alloys. Various Additive manufacturing (AM) techniques have been the subject of magnesium research in recent years because of many advantages over conventional technologies, such as free forming and complex shapes manufacturing with excellent dimensional stability and high material efficiency^{4,10}.

¹Institute of Machine and Industrial Design, Faculty of Mechanical Engineering, Brno University of Technology, Czech Republic; ²Institute of Materials Science and Engineering, Faculty of Mechanical Engineering, Brno University of Technology, Czech Republic; ³Computed Tomography Research Group, University of Applied Sciences Upper Austria; email: Jakub.Slavicek1@vut.cz

One of the most explored AM techniques for metals is Laser powder bed fusion (LPBF). Although the research on magnesium alloys shows good results^{11,12}, LPBF is connected with high machine cost, size limitation, complicated process optimisation, powder handling and storage with its safety concerns. Moreover, magnesium alloys with low melting point temperature elements are highly susceptible to evaporation due to localised heat, and process complications due to melt pool instability^{11,13}.

Another AM technique highly preferable for the deposition of Mg alloys is Wire Arc Direct Energy Deposition (WA-DED), also called Wire Arc Additive Manufacturing (WAAM). This process utilises a wire feeder system, an electronic arc heating source and an industrial robot. During the process, filler metal wire, shielded by inert gas, is heated through an electric arc and deposited as a bead on the base material. A controlled atmosphere chamber is not required, leading to more efficient use of shielding gas. WADED is widely used in rapid prototyping of large parts because of its high deposition rate, high material utilisation rate and low cost^{2,6,14,15}. Unlike the LPBF technique, WADED is not constrained by platform or build chamber size. However, arc-based additive manufacturing presents challenges, as several process parameters must be monitored, and optimisation is necessary¹⁴. That is crucial to addressing common WADED challenges, including insufficient or excessive penetration, residual stress, deformation caused by high heat input, reduced dimensional accuracy, formation of cracks and porosity^{15,16}.

Regions with increased porosity in the welds are formed mainly due to hydrogen, either as an impurity in the weld material and/or base metal or from the air humidity. The magnesium surface is covered by magnesium oxide when exposed to the atmosphere. If moisture is present, the oxide is converted to magnesium hydroxide¹⁷ which can be easily introduced to the melt pool during welding. The hydrogen solubility in molten magnesium is relatively high and decreases substantially during cooling, resulting in the formation of pores¹⁸. Such inhomogeneity can act as a stress concentrator, reducing the mechanical performance of the final product. Also, when internal stresses, caused by the high coefficient of thermal expansion of magnesium, are generated during the welding process, cold cracks can initiate from the pores in solidified weldments.

The formation of cold and hot cracks when welding magnesium alloys is a topic that has been widely discussed in connection with WADED technology^{9,10,19,20}. Various studies have shown that crack size and susceptibility to crack formation increase with the magnitude of electric current and heat input¹⁰. Also, higher aluminium content in magnesium alloys can increase susceptibility to cracking^{9,19,20}. Hot welding cracks in magnesium alloys can be formed by various mechanisms. During solidification, when part of the weld metal is already solidified, but regions with higher concentrations of alloying elements are still in the liquid form, internal stresses can result in cracking on the interface. Similarly, cracks are formed in the heat-affected zone on the interface between solid solution and liquified low-melting-point phases. That is especially important for the WADED process, because previously deposited layers are affected in the same manner as the heat-affected zone during the building process. Furthermore, it was experimentally proven that multiple thermal cycles, simulating multiple welding passes, increase internal stress and hot cracking susceptibility in AZ magnesium alloys¹⁹.

In contrast to using a conventional power source, the Cold Metal Transfer (CMT) process, in which the wire is retracted after the short circuit, effectively mitigates the defects mentioned above due to its controlled heat input²¹. This sustainable method reduces heat input by approximately 33% compared to conventional welding power sources and minimises spatter²².

In addition to defects, different layer widths have been observed in thin-walled parts during WADED fabrication²³. This observation was related to the temperature change of the base material, which can heat up to 150 °C during the fabrication. The change in temperature occurs during the production of the first few layers. After that, the temperature settles to a certain level, and the width of the layers remains stable.

The electric arc welding process causes a large thermal gradient. Therefore, residual stresses inside the thin-walled parts are produced by WADED¹⁶. The stresses then further cause deformation of the part. The magnitude and location of the maximum residual stresses depend on the dimensions of the base

material, the number of layers, or the parameters set on the welding source²⁴. It has been shown that increasing the interpass temperature to 100°C can reduce the internal stresses by up to 20%.

These findings suggest that aspects that arise in magnesium alloy WADED, such as defects, thin-walled part geometry, and residual stresses, depend on the magnitude of the thermal input and the temperature of the base material. It has been shown that by the use of preheating, the mechanical properties of magnesium alloy welded joints can be enhanced²⁵. Therefore, preheating can potentially improve the quality of WADED-fabricated parts.

Three experiments were conducted in this study. The first experiment investigated the change in geometry of the single-track weld bead due to preheating of the base material by a heated table. Based on the first experiment's results, the second experiment was conducted to investigate the possibility of using preheating to compensate for the differences in layer widths in fabricating a thin-walled part. For this, two strategies for using preheating in WAAM fabrication were proposed. Finally, the third type of experiment investigated whether reducing the residual stress inside thin-walled parts is possible by preheating the base material.

Materials and methods

All welding experiments were carried out using Cold Metal Transfer (CMT) power source Fronius TPS 3200 CMT paired with KUKA KR 60 HA 6-axis robotic arm controlled by Rhinoceros 6 software. During the tests, a constant speed of the welding torch (WS) of 10 mm/s and a distance from the manufactured part of 13 mm was maintained. Pure argon (99.5 %) was adopted as the shielding gas with a flow rate of 18 l/min. The AZ61 wire with a diameter of 1.6 mm and chemical composition given in Table 1. was used as filler material. In the preceding study²⁶, which formed the basis of this work, the filler wire was manually cleaned with SiC paper. The present research streamlined the preparation process by employing a custom-built automatic rotary device to remove surface impurities. Following mechanical cleaning, the wire was annealed at 380 °C for 11 minutes to convert residual magnesium hydroxide into less WADED affecting magnesium oxide¹⁸. Base material was mounted on the custom preheating table with overall dimensions of 450x550 mm, an output of 3.2 kW and a maximum preheating temperature of 400 °C with precision of ± 1 °C.

Elements	Al	Zn	Mn	Si	Fe	Cu	Ni
Max%	6.50	1.50	0.40	0.10	0.005	0.05	0.005

Table 1. Chemical composition of AZ61 magnesium alloy wire

Filler material (wire) and cross-section specimens from single-tracks and thin walls were used for metallographic observation. Samples were prepared in usual way, ground with SiC papers and polished with diamond pastes. Some samples were etched using an etchant based on acetic and nitric acid to reveal microstructural features. Optical microscopes, Olympus SZX7 and Zeiss Axio Observer Z1m, were used for observation and documentation. Due to the presence of γ phase on grain boundaries, grain size was evaluated manually using the line intercept method and image analysis software ImageJ. A scanning electron microscope with a field emission gun, Zeiss AG Ultra Plus, was used for more detailed observation and chemical analysis.

Single track samples

The influence of preheating of the base material on the bead geometry was tested in the range of 20°C–350°C. Two sets of eight single-track samples each were fabricated. Each sample was fabricated at different preheating temperatures, namely 50°C, 100°C, 150°C, 200°C, 250°C, 300°C and 350°C, including a reference sample fabricated without preheating. Samples were fabricated on AZ31 alloy base plates, and each single-track weld bead was 50 mm long. The first set of single tracks was produced using

the reference parameters (REF), established in previous research²⁶. Parameters for the second set were selected to accomplish a greater depth of penetration (DWP). Unlike the earlier study, the base material used was the AZ31 alloy, which requires an adjustment of the parameter and preheating combination to achieve the desired penetration along the entire interface between the base material and the deposited layer. The specific REF and DWP parameters used are listed in Table 2.

After production, an optical 3D scanner (ATOS Triple Scan III) was used to measure all samples. Based on the scanned data, the height and width of the weld bead were evaluated using the software GOM Inspect 2018. The width and height of the weld bead were measured in six sections through the central part of the sample. Cross-section samples were prepared for further examination of weld penetration depth. Three cross-sections from the central part of each single-track weld bead were cut and prepared for metallographic observation. The samples were used to observe the effect of preheating on the depth of the weld bead and to identify a suitable combination of preheating and process parameters.

Parameters description	Abbreviation	I_boost	t_I_boost	I_sc_wait	vd_sc_wait	I_sc2
Reference parameters (developed in prev. study)	REF	430 A	2,5 ms	30 A	30 m·min ⁻¹	50 A
Deeper weld penetration parameters	DWP	400 A	3,5 ms	30 A	30 m·min ⁻¹	50 A

Table 2. CMT parameters used for WADED

Layer width stabilisation samples

In the next step, thin-walled samples with a length of 50 mm, consisting of 15 layers, were fabricated for the width compensation experiment. AZ31 alloy was used as a base material, and the layer height was set to 2.6 mm. At first, two samples were fabricated without preheating to determine the width change with increasing number of layers. The width of the layers was measured using an optical 3D scanner (ATOS Triple Scan III) and evaluated at 15 levels with an offset of 2.6 mm.

Two strategies were proposed for preheating optimisation. For the first strategy, the base material was preheated to 200 °C and the thin-wall was fabricated with an interpass temperature of 200 °C. For the second strategy, the base material was preheated to 200 °C, three layers were fabricated with an interpass temperature of 200 °C and the rest of the sample was manufactured with an interpass temperature of 50 °C. The number of layers fabricated with a higher interpass temperature was chosen based on the width changes observed in thin-walled parts fabricated without preheating. The first three layers of the thin-walled sample showed the most significant difference in width.

Residual stress and porosity samples

Based on the results from previous steps, thin-walled samples with a length of 60 mm, with a layer height of 2.6 mm, consisting of 10 layers, were fabricated with preheating temperatures from 50 °C to 300 °C. Interpass temperatures were equal to the preheating temperature for the fabrication of the whole sample. As base material, AZ31 alloy plate with dimensions of 90x15x10 mm was used and mounted only on one side to the preheating table to measure deformation in the produced samples (see Fig. 1). The base material was mounted on a heated table and scanned using a handheld optical scanner (Scantech SIMSCAN 22). Subsequently, a thin-walled sample was produced and allowed to cool down to room temperature. Then, the thin-walled sample fabricated on the base material was scanned again. Both scans were aligned and measured using GOM Inspect 2018 software. The deformation of the underside of the base material

was observed. This plastic deformation of the base material occurs due to residual stresses caused by a large temperature gradient in the material. The measured deformations can be used for comparative analysis of the amount of residual stresses in the material at different preheating temperatures.

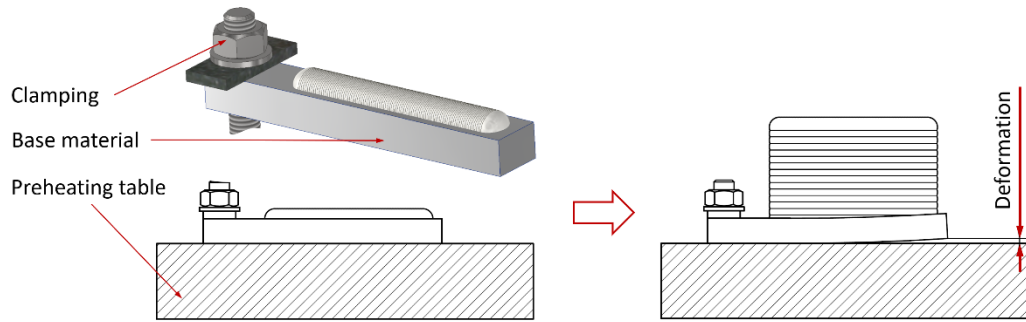


Fig. 1. Thin-walled specimen used for analyzing residual stress-induced deformation

The thin-walled samples were inspected using a μ CT system (Procon CT-Alpha) to analyse the relative material density. Specimens were scanned at a $45\ \mu\text{m}$ isometric voxel size resolution using a cone beam μ CT device. The voltage was set to 230 kV while the applied current was $200\ \mu\text{A}$. A copper filter was used to minimise beam hardening effects. The pore distribution, shape, and size were evaluated using the VGStudioMax 2023.1 (Volume Graphics), using an ISO50 threshold and a minimum of eight voxels for a segmented pore. These parameters provide information about porosity formation during WADED production.

Results and discussion

Geometry of the single-track weld bead

The measurement results regarding the influence of base material preheating temperature on the geometry of a single-track weld bead indicate that increasing the preheating temperature leads to an increase in bead width and penetration depth, while reducing the weld bead height. The results and selected cross-sections of the weld bead preheated to a temperature of 250°C are shown in Fig. 2. Two parameter sets were tested as part of the single-track weld geometry measurement. The reference parameters (REF) are based on a study where AZ91 base material was used. The base material used in this study is AZ31, which is why the weld penetration depth measurements showed very low values with REF parameters. For this reason, a set of parameters for deeper weld penetration (DWP) was also tested.

The weld bead height decreased from 4.08 mm to 2.75 mm (32.6%) for REF parameters and from 4.25 mm to 4.16 mm (2.1%) for the DWP parameters as can be seen in Fig. 2a. The results show that the DWP parameters with lower I_{boost} current and its longer duration result in a slower downward trend and significantly reduce the influence of preheating on decreasing weld bead height.

The effect of preheating on the weld width is very significant for both welding parameter sets. The weld width of the REF samples increased from 7.23 mm to 11.3 mm (56.4%) and from 9.18 mm to 12.19 mm (32.8%) for DWP samples. Both curves in Fig. 2b. show a similar growth trend and similar standard deviations, indicating comparable weld width stability.

The samples produced with the REF parameter settings did not achieve sufficient penetration depth until preheating to 100°C (Fig. 2c). Up to this temperature, weld penetration occurred only locally along the length of the weld bead and cohesion with the base material was minimal. Stable penetration depth was observed from a preheating temperature of 150°C to 350°C , where the penetration depth increased from 0.3 mm to 1.15 mm. Additionally, samples preheated to a temperature below 200°C showed a higher pore concentration at the interface between the weld bead and the base material, which was probably caused by surface contaminants or corrosion residues⁷.

For the DWP samples, the parameter change resulted in a significant shift in the penetration depth. In the sample without preheating (20°C), the penetration depth was 0.37 mm, and gradually increased to 2.26 mm for a preheat of 350°C. The weld penetration depth growth trends in Fig. 2c are similar for REF and DWP parameters. A significant standard deviation can be observed for DWP parameters. This indicates poor weld penetration stability along the weld length. For a preheat temperature of 250°C, sufficient weld penetration depth is achieved using REF and DWP parameters as seen in Fig. 2d.

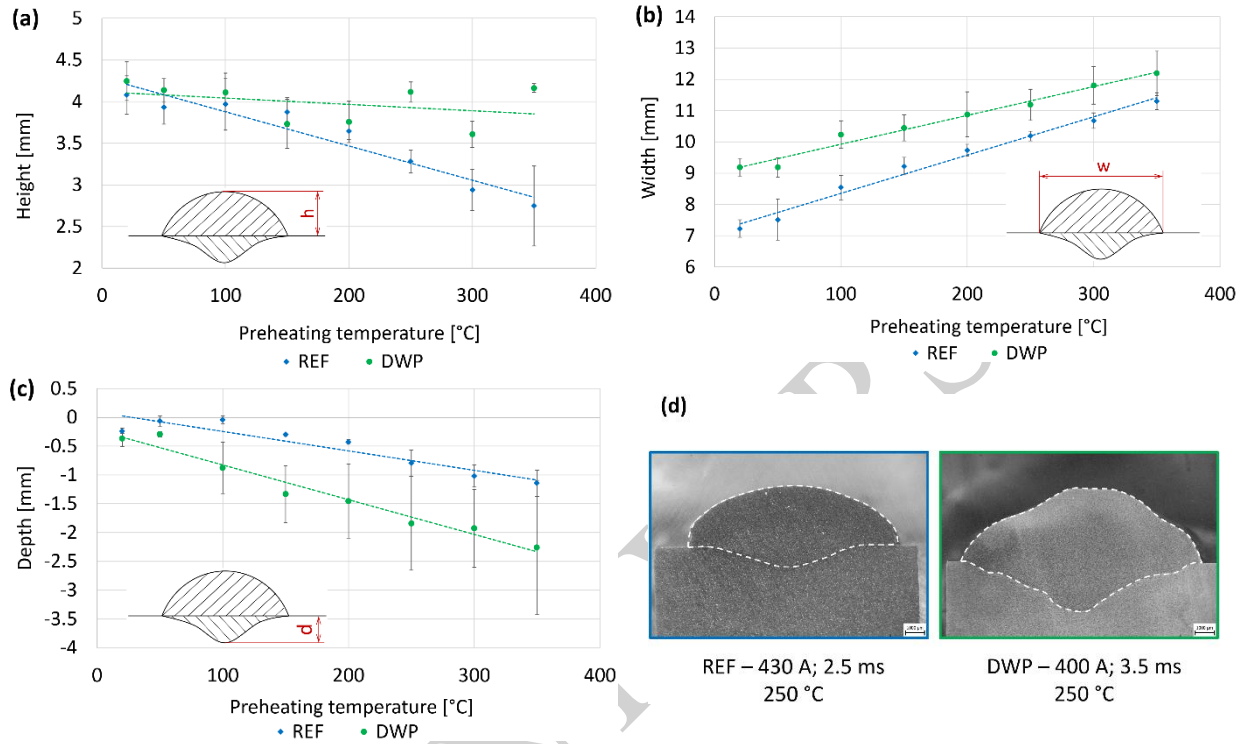


Fig. 2. (a) Height (b) width (c) penetration depth of single-track weld bead (d) cross-section of selected samples

Layer width stabilisation

This experiment aimed to eliminate wall necking in the first layers of thin wall caused by enhanced heat sinking through the base plate within the first few layers²⁷. In the first phase of this experiment, two thin-walled samples with different parameters (REF, DWP) were produced to verify the suitability of the parameters for the production of thin-walled parts and to identify expected defects (see Fig. 3a). Subsequently, two more samples were produced using REF parameters. These samples were focused on evaluating the preheating method (see Fig. 3b). One sample was fabricated with preheating of 200 °C lasting the entire production time and an interpass temperature of 200°C. The second sample was produced with preheating of 200°C for the first three layers, followed by no preheating with an interpass temperature of 50 °C.

The width of the first layer of a thin wall produced without preheating with DWP parameters corresponds to 10 mm, the average wall width is 15.5 mm, so the percentage increase is 54.4%. This narrowing is significant and cannot be compensated by the preheating alone. In addition, the wall produced with DWP parameters exhibits significantly unstable behaviour across the height of the sample. For this reason, the DWP parameters were assessed to be unsuitable for producing multi-layer thin walls. They were not used for the production of further samples. The width of the first layer of a thin wall produced without preheating with REF parameters corresponds to 7.9 mm, the average wall width is 8.6 mm, and the percentage increase is 8.7%. The observed necking can be compensated by preheating. According to the

single-track experiment, the first weld should reach the required width already at a preheating temperature of 150 °C. However, due to insufficient penetration depth during preheating at 150 °C while using REF parameters, a minimum suitable preheating temperature of 200 °C was selected. This temperature should ensure the minimum required penetration of the base material and, at the same time, sufficient width of the first layer.

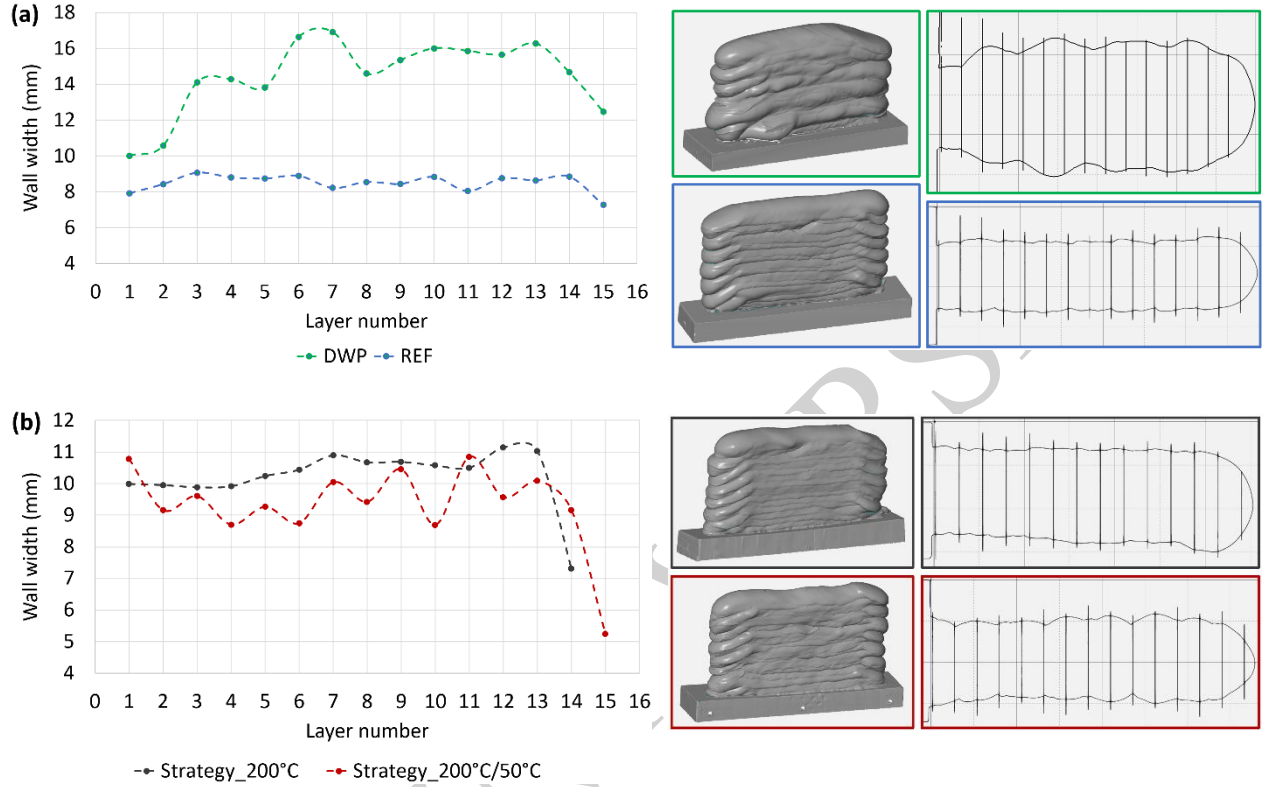


Fig. 3. Preheating of thin walls to eliminate necking, a) REF and DWP parameters without preheating, b) REF parameters with preheating at 200°C and 200/50°C

The sample produced with preheating and an interpass temperature of 200 °C (Strategy_200°C) showed a stable layer width with no significant difference between the first and remaining layers (see Fig. 3b). The width of the first layer was 10 mm, the average layer width was 10.3 mm, and the percentage increase was only 3.2%. At the same time, a reduction in the height of the individual layers was observed, which led to a decrease in the overall height of the sample, which was 34.6 mm. For comparison, the height of the sample produced with REF parameters without preheating was 39.5 mm. When using sample preheating to 200 °C for only 3 layers, followed by production with an interpass temperature of 50 °C (Strategy_200/50°C), a slight decrease in layer width was observed after the third layer from 10.8 mm on the first layer to 8.7 mm, with an average layer width of 9.5 mm, corresponding to a percentage reduction in width of 17.5%. Overall, this strategy led to poorer layer width stability across the sample height than the first production strategy, with an interpass temperature of 200 °C for the entire sample. On the other hand, there was no significant reduction in layer height, and the final sample had a height of 38.3 mm. It was 3.6 mm higher than the sample produced by Strategy_200°C and 1.2 mm lower than the sample with REF parameters without preheating.

While a preheating and interpass temperature of 200°C stabilises the layer width and prevents necking at the bottom, it also reduces the layer height. This should be considered when planning trajectories for producing taller thin walls, mainly to keep the contact tip at a constant distance from the fabricating thin wall.

Residual stress

Six thin-walled samples with REF parameters and preheating temperatures of 50, 100, 150, 200, 250, and 300 °C were produced to describe the effect of preheating the base material on internal stresses. The results are shown in Fig. 4. Since measuring the amount of residual stress is challenging, a comparative method was used to determine the manifestations of internal stress in the form of deformation of the base material. Details of the conditions used for sample production are provided in the Materials and methods section.

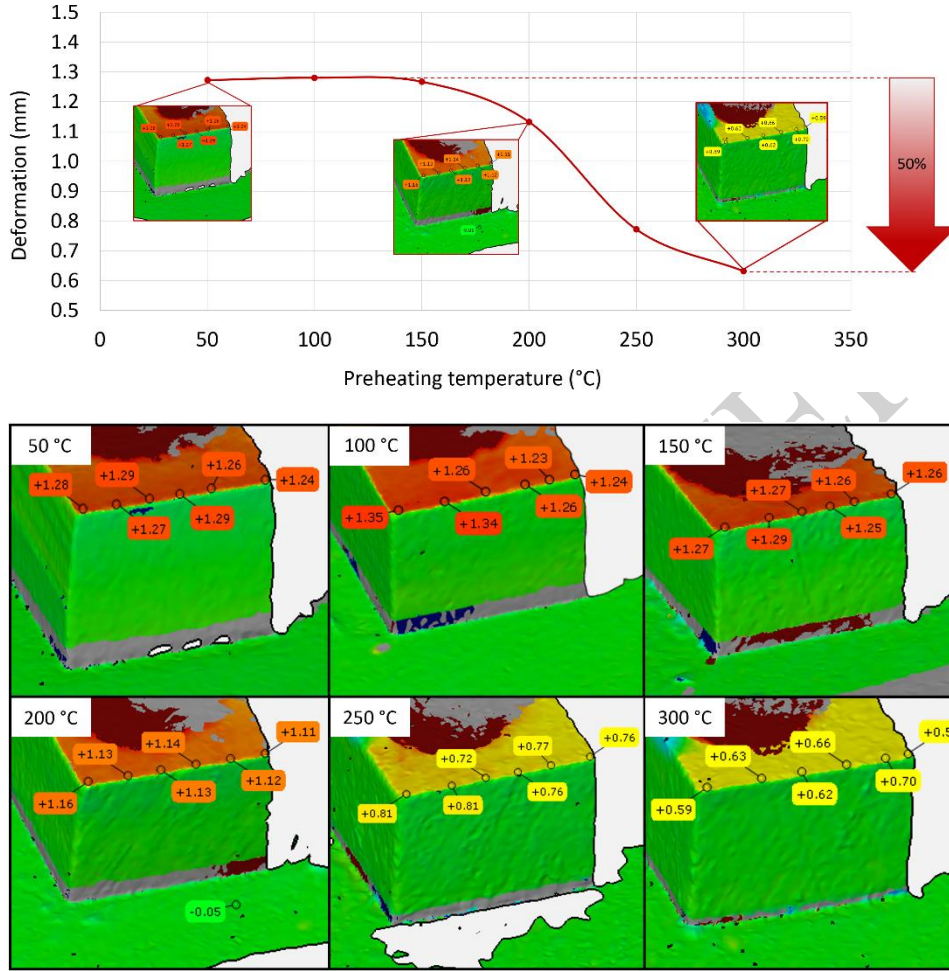


Fig. 4. Effect of preheating on the internal stress - deformations measurement

The results of the deformation measurements show that up to a temperature of approximately 150 °C, preheating has no effect on the amount of residual stress remaining in the thin-walled body. In this temperature range, the maximum measured deformation was approximately 1.27 mm. In the range from 150 °C to 300 °C, a significant reduction in deformation and thus in the amount of residual stress in the body was observed. At a preheating temperature of 200 °C, the deformation decreased to 1.13 mm, and at 250 °C to 0.77 mm. At the maximum tested preheating temperature of 300 °C, a deformation of 0.63 mm was measured. At this preheating temperature, a reduction in deformation of up to 49.6% was achieved. From the shape of the curve interpolated by the measured points, it can be assumed that the results asymptotically approach a value outside the investigated preheating temperature range. Higher preheating temperatures would probably not lead to further significant reductions in deformation and thus residual stress.

Due to using a new approach to preparing filler material for WADED production, porosity and microstructure were observed on the same samples as for residual stress. The purity of the input material significantly affects the amount of porosity contained in the samples, and the measured results show a significant influence of the preheating of the base material on the amount of porosity. The μ CT images of individual samples with different preheat temperatures are shown in Fig. 5. The highest porosity level, 2.1%, was observed in the sample preheated to 50 °C. The lowest porosity of 0.01% was measured in the sample preheated to 250 °C. In general, overall porosity decreased with increasing preheating temperature. All samples contain small pores in the interlayer region. Moreover, samples preheated to lower temperatures exhibited large columnar pores extending across multiple deposited layers. To the best of our knowledge, such internal defects were not reported in the literature before, and further analysis is presented in the following sections.

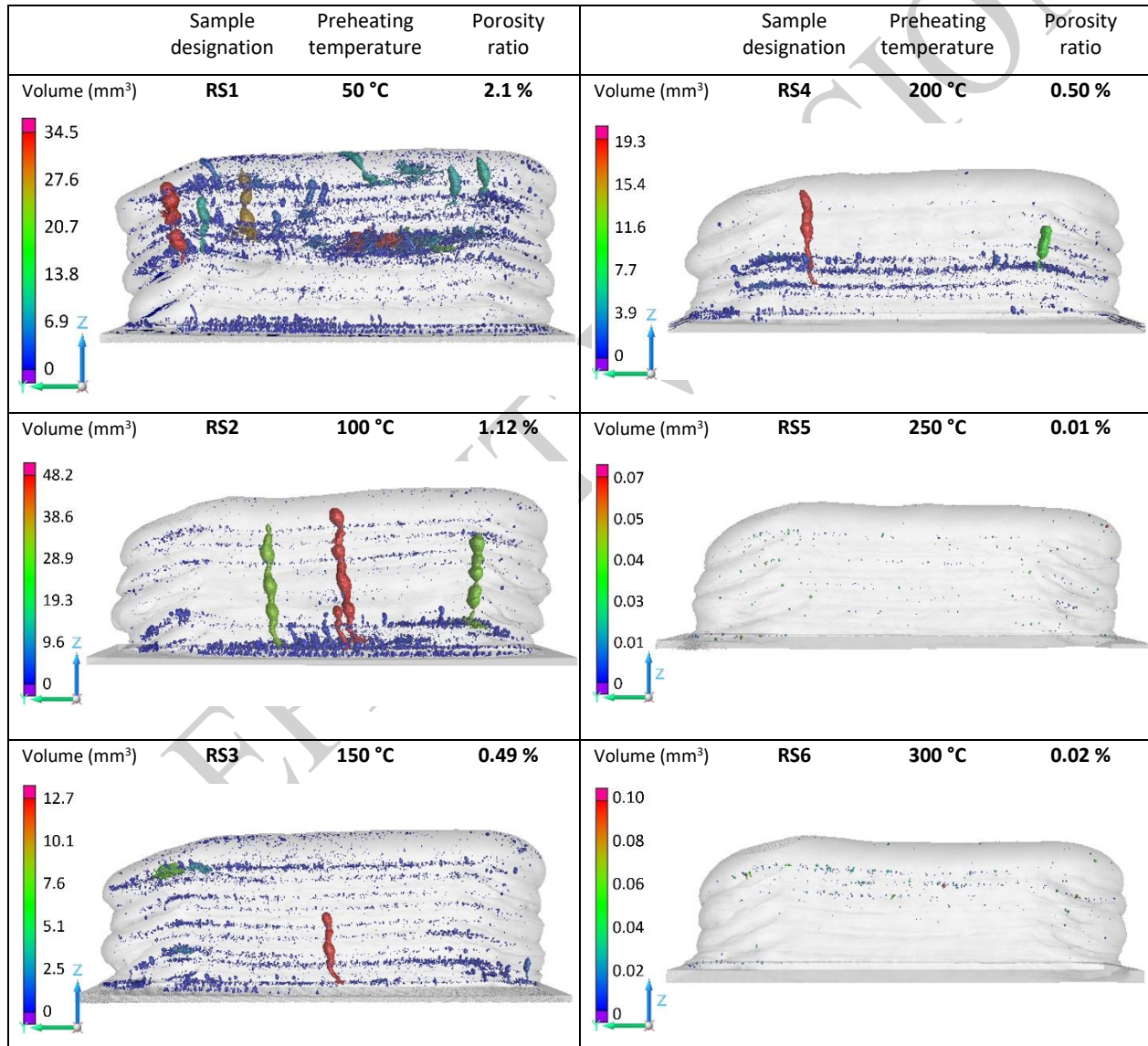


Fig. 5. Porosity measurement using μ CT scanning

All fabricated samples exhibited a layered macrostructure with a distinct interface containing coarse grains (CG) followed by very fine grains (FG). The macro and micro morphology of samples fabricated with

preheat temperatures of 250 °C and 100 °C are shown in Fig. 6. Those samples were chosen specifically because the preheat temperature of 250 °C is the lowest temperature resulting in the elimination of columnar pores and low interlayer porosity. On the other hand, the sample fabricated at a preheat temperature of 100 °C contained interlayer porosity, several columnar pores, and sizable globular pores. The sample fabricated with a higher preheat temperature was fairly symmetrical; only half of the image is presented. On the contrary, the sample fabricated at a lower temperature was asymmetrical; the presence of columnar and large globular pores resulted in layer height and width variations.

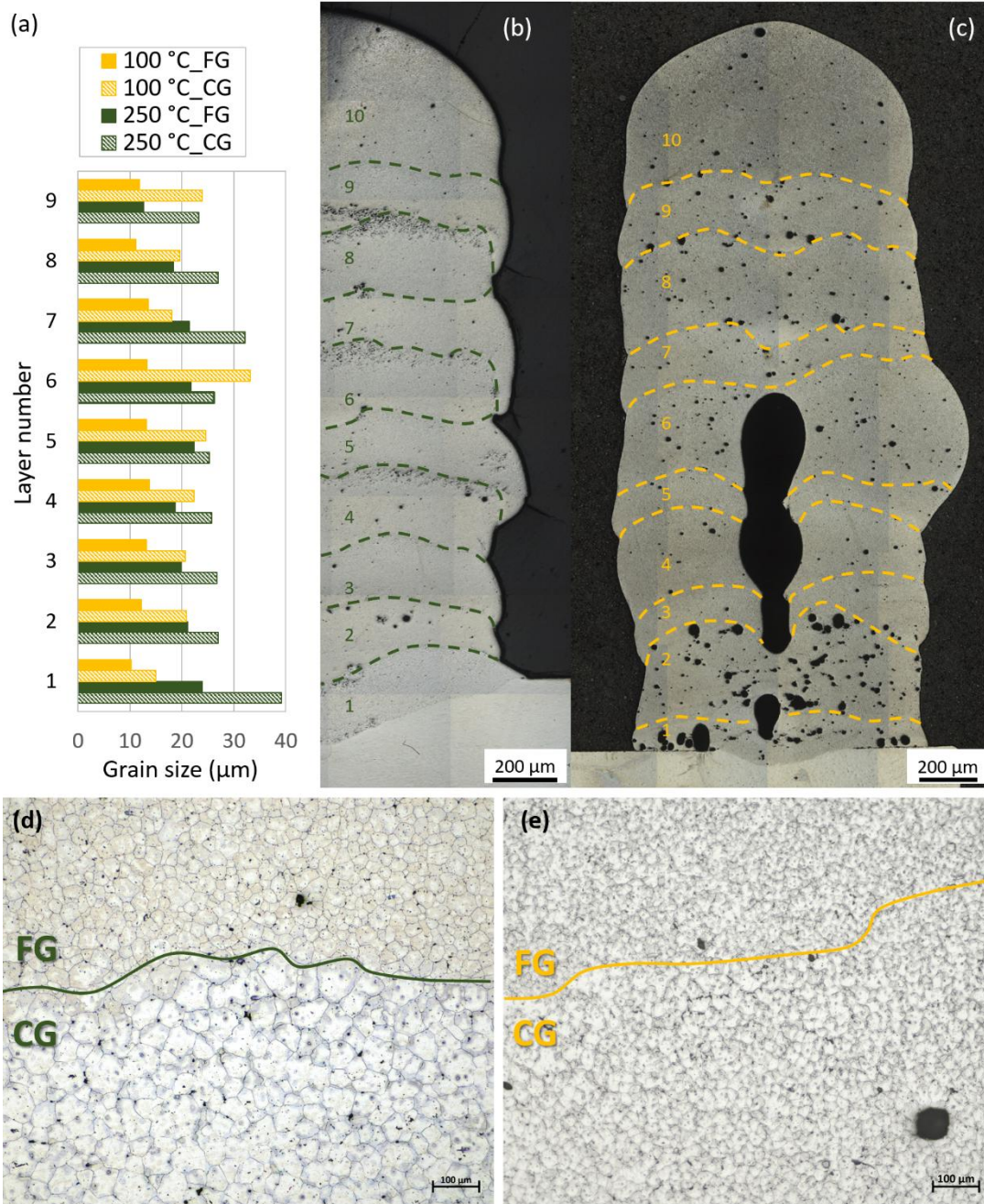


Fig. 6. Thin wall samples fabricated with preheating: (a) grain size in fine grain (FG) and coarse (CG) areas in individual layers; overall macro images of samples fabricated with preheat temperature of (b) 250 °C and (c) 100 °C; microstructures on the 1-2 layer interface of sample fabricated with preheat temperature of 250 °C and (e) 5-6 layer interface of sample fabricated with preheat temperature of 100 °C

Microstructural observation of all samples fabricated with different preheat temperatures showed similar microstructures, such as solid solution, Al-Mn-based particles and $Mg_{17}Al_{12}$ phase, with significantly higher amounts precipitated in the top part of the samples. Depending on preheat temperature, an increase in $Mg_{17}Al_{12}$ phase quantity started between layers 5 and 7. Similarly, differences in grain sizes were observed in individual layers, as seen from the grain size-layer number dependence in Fig. 6a. Each layer starts with a fine grain region (FG) and ends with a coarse grain region (CG). In a sample fabricated at a preheat temperature of 100 °C, the FG size varies between 10.24 and 13.71 μm , with stable values in the middle part of the sample and slightly smaller grains in two layers in the top and two layers in the bottom of the sample. The CG size, on the other hand, was very low in the first layer (15.01 μm) and gradually increased up to the sixth layer (33.19 μm). It should be noted that the size difference between the fifth and sixth layer was 26% and the difference between the sixth and seventh layer was 46%. Finer grains in the first layer can be attributed to the effective cooling by heat transfer to the base plate, which was preheated to 100 °C. In comparison, the maximum temperature measured on the sample was ~ 350 °C.

In the sample fabricated at a preheat temperature of 250 °C, the tenth layer contained the finest grains. In contrast, the first layer contained grains of the largest size, in both the CG and FG regions. The middle part of the sample was formed by grains with sizes oscillating around 20.5 μm and 27 μm for the FG and CG regions, respectively. High values in the first layer were caused by less effective heat transfer to the base plate, which was preheated to a relatively high temperature. Also, relatively high interpass temperature resulted in higher maximum temperature measured on the sample, namely ~ 470 °C. Fine grains in the top resulted from more effective cooling, which was least affected by the rest of the sample.

Grain sizes in all fabricated samples measured on the 3-4 (bottom) and the 8-9 (top) layer interfaces are shown in temperature dependence in Fig. 7. These specific layers were chosen as the grain size should not be affected by the position on the sample, i.e. by the peak values in the first layers or 5-6-7 layer interfaces. As can be seen from the results, grain size coarsening follows the same trend in the top and bottom areas. Most results comparing both areas show similar results with differences within the standard deviation, except for the peak value in the bottom CG area of the sample fabricated at 300 °C preheat and interpass temperature.

Grain size in the first layers and grain size in the top and bottom areas were clearly affected by the preheat temperature. When preheat and interpass temperatures were low enough to allow sufficient cooling via heat transfer to the base plate, the overall temperature of the sample was lower. The maximum temperature measured on the sample without preheating was ~ 260 °C, and every 50 °C increment in preheat and interpass temperature caused an increase in maximum sample temperature by 40 – 50 °C. As was reported by Chen et al.²⁸, AZ61 alloy exhibits an insignificant increase in grain size at annealing temperatures up to 350 °C, even after a 25-hour dwell time. Higher annealing temperatures of 400 and 450 °C result in a steep increase in grain size. Therefore, we can expect that when the maximum sample temperature reaches over 400 °C, which corresponds to preheat and interpass temperatures of 200 °C, the grain size should slightly increase in the whole sample even after 30 minutes, which was the maximum fabrication time for the presented thin-walled samples. A more significant increase in grain size is expected in samples with maximum temperature over 450 °C, i.e. 300 °C preheat and interpass temperature. In addition, with higher preheat temperature, cooling is slower and the sample is held over the critical temperature for longer.

Appearance and the number of pores corresponded to observations using μ CT. Interlayer porosity, the number of small pores on the interface between individual layers, can be clearly visible in macrographs and micrographs in Fig. 6. The interlayer porosity is most likely caused by impurities present in the filler material. Magnesium is a highly reactive metal that readily reacts with atmospheric moisture, forming hydroxides on the wire surface. These hydroxides decompose when introduced into the melt pool, releasing hydrogen gas¹⁸. Due to the rapid solidification rate of magnesium, the gas does not have sufficient time to escape the molten pool, and surface tension traps it within the material, forming pores. When a higher

preheat temperature is used, the overall temperature of the sample increases, allowing for slower cooling and sufficient time for gas to escape before solidification of deposited layer.

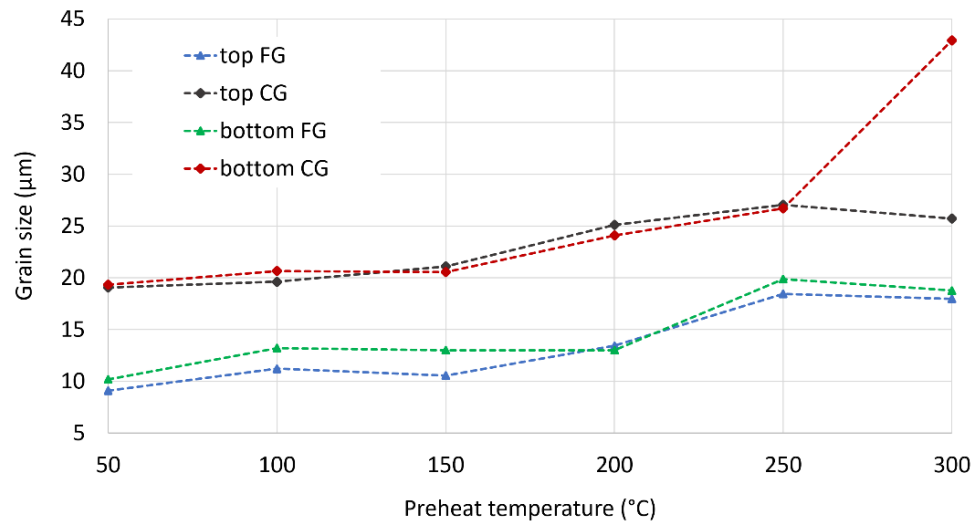


Fig. 7. Average grain size in the fine grain and the coarse grain regions in samples fabricated with different preheat temperatures

A similar mechanism would explain the shape of columnar pores (see Fig. 8). Firstly, a large pore is formed during the solidification of the deposited layer. During the deposition of subsequent layers, localised remelting can occur around the trapped gas, enabling it to migrate upward, resulting in vertical porosity channels tilted in deposition direction in every layer. These columnar pores were not observed in samples preheated to temperatures of 250 °C and higher, most probably due to the high overall temperature of the sample and slower solidification. On the other hand, no influence of lower preheat and interpass temperature can be observed, and the presence of columnar pores in the samples seems to be very random. This fact and the nonuniform distribution of interlayer porosity suggest that even though porosity can be minimised by technological means, it is not caused by process parameters or errors in deposition.

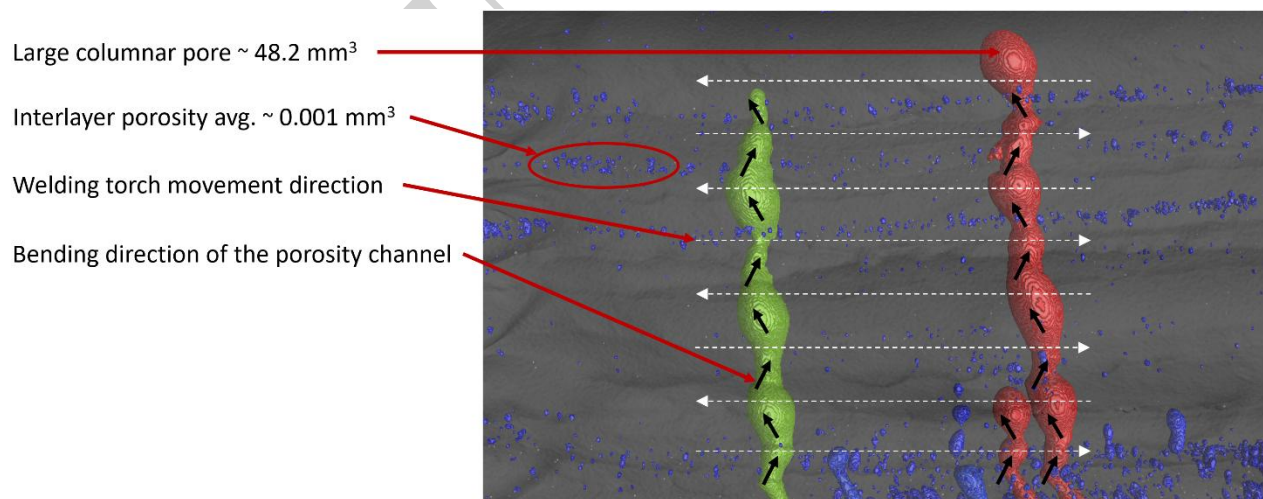


Fig. 8. Columnar porosity formation in a WADED thin-walled sample fabricated with preheat temperature of 100 °C

More detailed observation and chemical analysis were performed to explain the origin of columnar pores. As can be seen from secondary electron micrographs in Fig. 9, the surface of the columnar pore contained a high number of particles with sizes between 1.3 and 3.6 μm . Chemical analysis (Fig. 9d) confirmed the presence of aluminium and manganese in particles with no traces of iron. Even though the energy of Mn K β and Fe K α are very close, the absence of signal at 7.058 keV, the energy of Fe K β , proves that the last peak in the spectrum belongs to manganese.

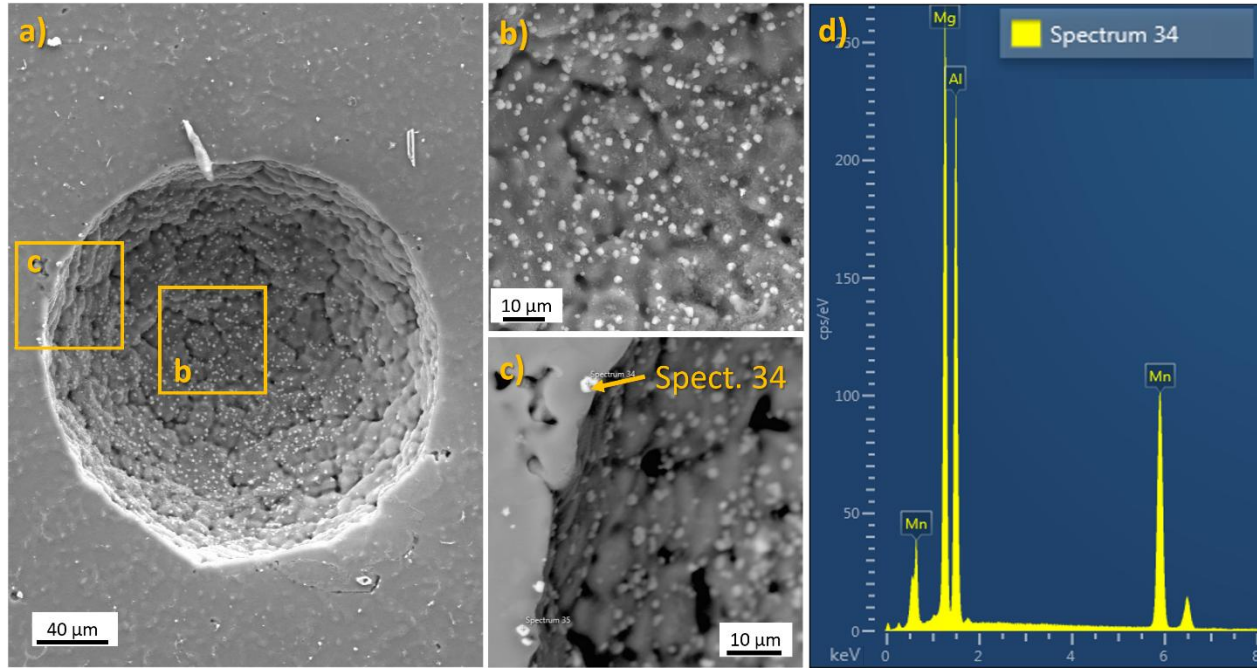


Fig. 9. (a) SEM image of columnar pore in sample fabricated with preheat and interpass temperature of 100°C, (b), (c) detailed images of particles, (d) energy dispersive X-ray spectrum of particle marked in image (c)

Further surface analysis along the columnar pore was performed to explain the presence of high amounts of secondary particles on the pore surface. Besides Al-Mn particles, higher amount of oxygen and locally traces of calcium were observed, as can be seen from image of representative area in Fig. 10. Elemental maps of Mg and Zn are not presented as the signal was detected all over the mapped area on the sample with no visible deviations, except for Al-Mn particle in central part, where less signal for Mg K α was detected.

Higher amount of Al-Mn particles could be explained by oxide layer on the pore surface. A similar phenomenon is documented in AZ alloys castings^{29–31}, where clusters of Al-Mn-based particles are attached to entrained oxide films. Particles in molten metal are either entrapped by entrained oxide or nucleate on entrained oxide and grow during cooling. During the WADED process, when a layer is deposited and part of the previous layer with a sizeable pore is remelted, the oxide film from the pore surface can act as entrained oxide and result in entrapment and/or nucleation of Al-Mn particles in the melt pool.

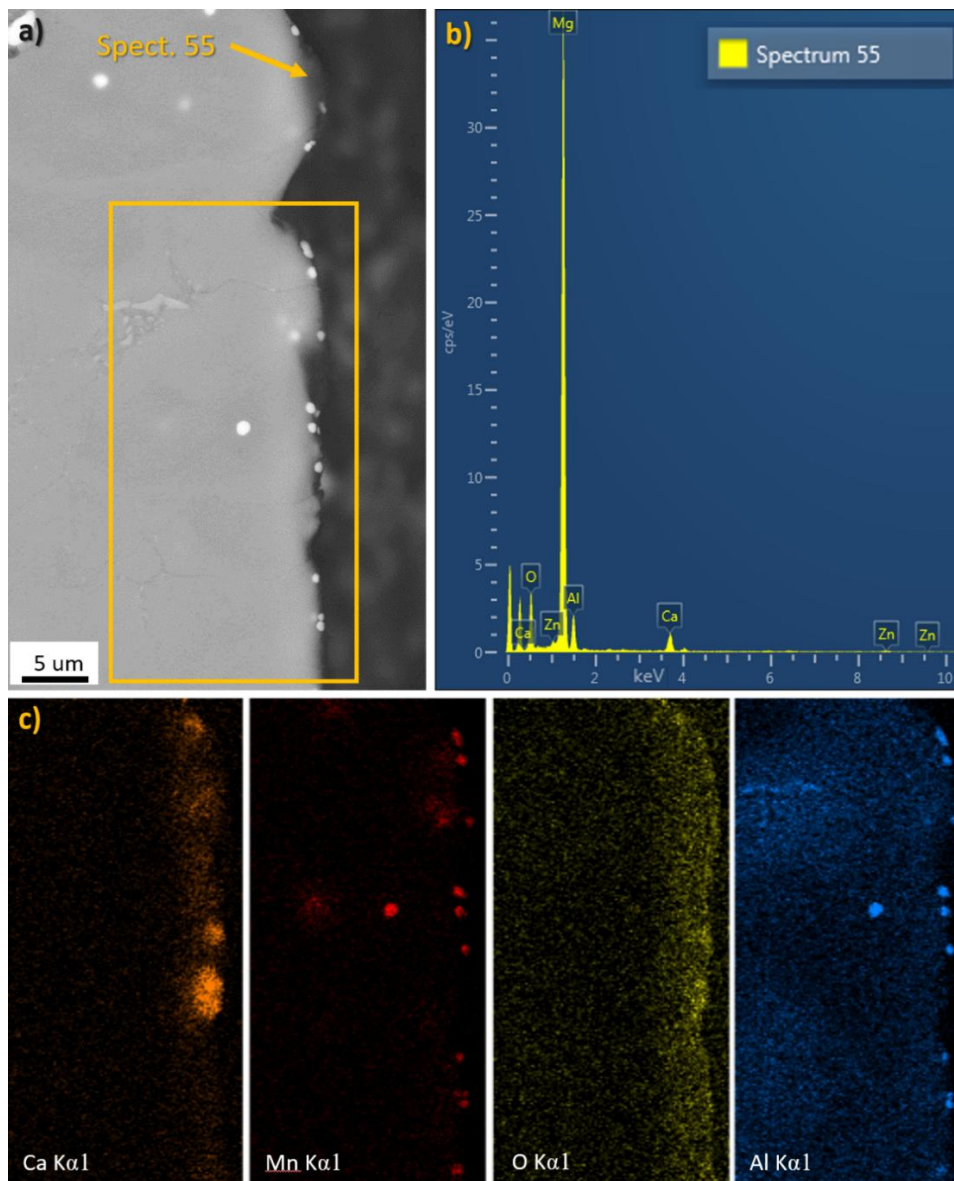


Fig. 10. (a) SEM image of the side of columnar pore with (b) energy dispersive X-ray spectrum of spot marked in image and (c) elemental mapping of marked area

Traces of Ca were observed only on the surface of the columnar pores, suggesting a deposition process as its origin, with three possible sources of contamination: shielding gas, base material and filler material. Shielding gas was supplied by a verified supplier, and no columnar pores or other contaminations were observed in other experiments while using the same batch of shielding gas. Since the columnar pores start in different layers in the thin-wall samples, we can also exclude the influence of the base material. To confirm the origin of Ca on the surface of the pore, filler wires were analysed (see Fig. 11). As the wire after pre-treatment did not show any traces of Ca, thick oxide layer or other contaminants, analysis of the wire without pre-treatment is presented. Microstructural components in filler wire were consistent with the microstructural analysis of thin wall deposits, but analysis of wire surface revealed higher amount of oxygen and locally traces of Calcium (see Fig. 11c). Calcium as part of surface oxide layer most probably

comes from lubricants used in wire drawing processes, in which calcium stearate is very widely used³² and entered the deposition process as a result of an insufficiently efficient pre-treatment of filler wire.

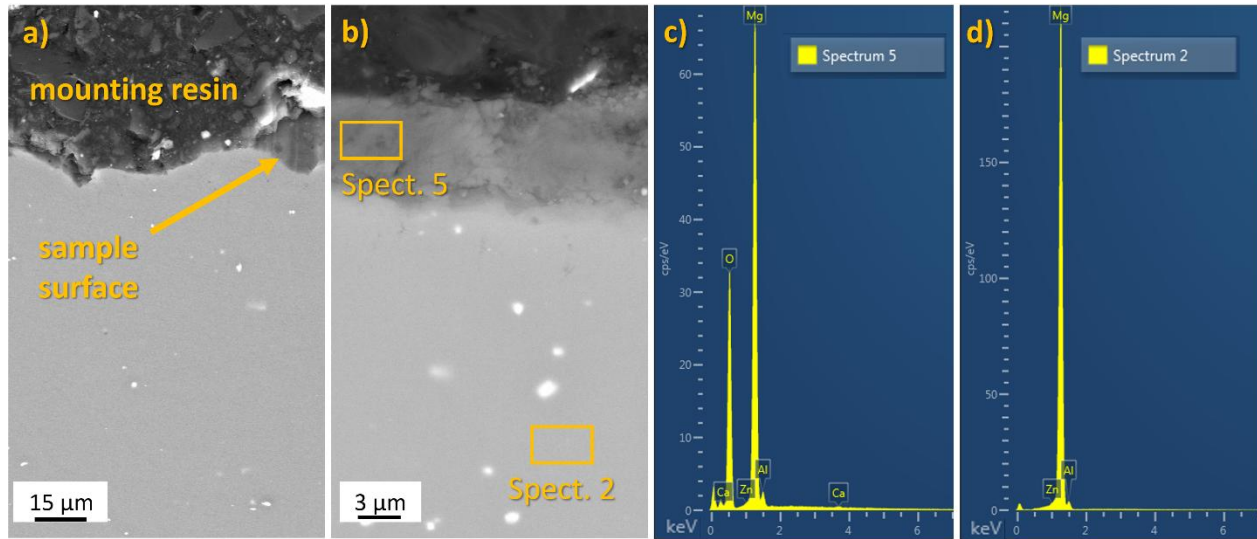


Fig. 11. SEM images of the wire (a) after pre-treatment and (b) before pre-treatment, (c) (d) energy dispersive X-ray spectra of areas marked in the image

The high reactivity of Mg causes an oxide layer on the wire surface. As expected, pre-treatment of the filler wire before deposition is mandatory. In our previous experiments, wires were prepared manually with SiC papers, which guaranteed a clean surface of the wire, and no columnar pores were observed in the produced samples. This study employed an approach that is more suitable for industrial applications. In the first step, the wire was mechanically cleaned by a custom-built automatic rotary device and then annealed to convert any remaining hydroxides into oxides. Even though the analysis of wire after pre-treatment did not reveal any oxides or contaminants, only a few randomly chosen pieces of wire were analysed, and further analysis of filler wire and optimisation of the process is necessary to ensure no impurities, such as Ca, can enter the deposition process.

Even though the automated pre-treatment process was not as effective as the manual process and resulted in severe material defects in thin-wall samples fabricated with lower preheat and interpass temperatures, the experiment proved that preheating can successfully diminish interlayer porosity. Results also suggest that preheating temperatures of 250°C and above can prevent columnar pores, but further examination is needed to prove such a hypothesis.

Although the preheating presents a higher production cost, it also significantly decreases the residual stress level and positively influences the thin wall geometry. A more effective automated pre-treatment process with sufficient preheating and interpass temperature is a promising method for producing thin-wall samples from AZ magnesium alloys by WADED.

Conclusion

This study confirmed that preheating and interpass temperature control are key to improving the quality of AZ61 magnesium alloy parts produced using the WADED method. Based on the findings, the following conclusions can be drawn:

- Preheating to 200 °C effectively stabilised layer width, eliminated necking in the initial layers, and ensured consistent part geometry throughout the build.
- Increasing the preheating temperature reduced deformation of the base material, corresponding to a residual stress decrease. The magnitude of deformation within thin-walled parts can be reduced by up to 50% using base material preheating.
- The amount and morphology of pores were strongly affected by preheating. While low preheating temperatures led to a high level of interlayer porosity and presence of columnar pores, these defects were almost completely suppressed at a 250 °C preheating temperature.
- The identified optimum range of 200–250 °C represents a balance between layer stability, stress reduction, and defect minimisation, making it suitable for practical application, depending on the specific requirements of the product properties.

Although this study was limited to relatively simple thin-walled specimens, the observations form a valuable basis for extending the approach to more complex shapes. The results can contribute to streamlining manufacturing workflows and supporting more sustainable production of magnesium alloys. A logical continuation of this work will be investigating mechanical properties and verifying the identified temperature window on geometries of higher structural complexity.

Author contributions

J.S. – Proposing research topic, conceptualization, methodology, data curation, investigation, writing – original draft, review & editing; S.Z. – methodology, investigation, writing – original draft; M.H. – methodology, investigation, writing – original draft; S.S. – technical and material support, methodology, investigation; D.K. – acquiring research funding; technical and material support, supervision.

Funding

This article presents research results that have received funding from the specific research project of faculty FSI-S-23-8340 and from project MEBioSYS - “Mechanical Engineering of Biological and Bio-inspired Systems”, funded as project no. CZ.02.01.01/00/22_008/0004634 by Programme Johannes Amos Comenius, call Excellent Research.

Acknowledgements

The authors would like to acknowledge the help of Jan Čupera for the SEM analysis.

Declaration of competing interests

The authors declare no conflict of interest.

Data availability statement

The data that support the findings of this study are openly available in Zenodo Repository at [10.5281/zenodo.16881884](https://doi.org/10.5281/zenodo.16881884).

References

1. Xie, H. *et al.* Recent progress on cast magnesium alloy and components. *J Mater Sci* **59**, 9969–10002 (2024).
2. Li, Y. *et al.* A Review on Wire Arc Additive Manufacturing of Magnesium Alloys: Wire Preparation, Defects and Properties. *Metals and Materials International* **30**, 3243–3267 (2024).
3. Yang, Y. *et al.* Research advances in magnesium and magnesium alloys worldwide in 2020. *Journal of Magnesium and Alloys* vol. 9 705–747 Preprint at <https://doi.org/10.1016/j.jma.2021.04.001> (2021).
4. Ning, H. *et al.* Understanding the deformation behaviours of Mg alloys with dispersed non-basal grain-embedded orientation heterostructures. *Acta Mater* **267**, (2024).
5. Liu, L. *et al.* Effects of Y and Zn additions on electrical conductivity and electromagnetic shielding effectiveness of Mg-Y-Zn alloys. *J Mater Sci Technol* **35**, 1074–1080 (2019).
6. Manjhi, S. K., Sekar, P., Bontha, S. & Balan, A. S. S. Additive manufacturing of magnesium alloys: Characterization and post-processing. *International Journal of Lightweight Materials and Manufacture* vol. 7 184–213 Preprint at <https://doi.org/10.1016/j.ijlmm.2023.06.004> (2024).
7. Ye, H., Yan, Z. L., Shen, B. & Xue, Z. F. Analysis on the weld defects of the AZ91D magnesium alloy joints. in *Materials Science Forum* vols 610–613 931–935 (Trans Tech Publications Ltd, 2009).
8. Tang, W., Mo, N. & Hou, J. Research Progress of Additively Manufactured Magnesium Alloys: A Review. *Jinshu Xuebao/Acta Metallurgica Sinica* **59**, 205–225 (2023).
9. Niknejad, S., Liu, L., Lee, M. Y., Esmaeili, S. & Zhou, N. Y. Resistance spot welding of AZ series magnesium alloys: Effects of aluminum content on microstructure and mechanical properties. *Materials Science and Engineering: A* **618**, 323–334 (2014).
10. Lang, B., Sun, D. Q., Xuan, Z. Z. & Qin, X. F. Hot Cracking of Resistance Spot Welded Magnesium Alloy. *ISIJ International* **Vol. 48**, 77–82 (2007).
11. Suchý, J. *et al.* Corrosion behaviour of WE43 magnesium alloy printed using selective laser melting in simulation body fluid solution. *J Manuf Process* **69**, 556–566 (2021).
12. Suchy, J. *et al.* Effect of laser parameters on processing of biodegradable magnesium alloy WE43 via selective laser melting method. *Materials* **13**, (2020).
13. Manjhi, S. K., R, O., Bontha, S. & Balan, A. S. S. Effect of burnishing strategies on surface integrity, microstructure and corrosion performance of wire arc additively manufactured AZ31 Mg alloy. *International Journal of Lightweight Materials and Manufacture* **8**, 355–373 (2025).
14. Rodrigues, T. A., Duarte, V., Miranda, R. M., Santos, T. G. & Oliveira, J. P. Current status and perspectives on wire and arc additive manufacturing (WAAM). *Materials* **12**, (2019).
15. Ding, D., Pan, Z., Cuiuri, D. & Li, H. Wire-feed additive manufacturing of metal components: technologies, developments and future interests. *International Journal of Advanced Manufacturing Technology* vol. 81 465–481 Preprint at <https://doi.org/10.1007/s00170-015-7077-3> (2015).
16. Ahmad, S. N. *et al.* FEM simulation procedure for distortion and residual stress analysis of wire arc additive manufacturing. in *IOP Conference Series: Materials Science and Engineering* vol. 834 (Institute of Physics Publishing, 2020).
17. Avedesian, M. M. & Baker, Hugh. *Magnesium and Magnesium Alloys*. (ASM International, 1999).
18. Wagner, D. C., Yang, Y. K. & Kou, S. Spatter and porosity in gas-metal arc welding of magnesium alloys: Mechanisms and elimination. *Weld J* **92**, (2013).

19. Huang, C. J., Cheng, C. M. & Chou, C. P. The influence of aluminum content of AZ61 and AZ80 magnesium alloys on hot cracking. *Materials and Manufacturing Processes* **26**, 1179–1187 (2011).
20. Huang, C., Cheng, C., Chou, C. & Chen, F. *Hot Cracking in AZ31 and AZ61 Magnesium Alloy*. *J. Mater. Sci. Technol* (2011).
21. Zeng, Z. *et al.* Recent progress and perspectives in additive manufacturing of magnesium alloys. *Journal of Magnesium and Alloys* vol. 10 1511–1541 Preprint at <https://doi.org/10.1016/j.jma.2022.03.001> (2022).
22. Wu, Q. *et al.* Obtaining uniform deposition with variable wire feeding direction during wire-feed additive manufacturing. *Materials and Manufacturing Processes* **32**, 1881–1886 (2017).
23. Guo, Y. *et al.* Formability, microstructure evolution and mechanical properties of wire arc additively manufactured AZ80M magnesium alloy using gas tungsten arc welding. *Journal of Magnesium and Alloys* **9**, 192–201 (2021).
24. Derekar, K. S. *et al.* Effects of Process Variants on Residual Stresses in Wire Arc Additive Manufacturing of Aluminum Alloy 5183. *Journal of Manufacturing Science and Engineering, Transactions of the ASME* **144**, (2022).
25. Shen, J. & Xu, N. Effect of preheat on TIG welding of AZ61 magnesium alloy. *International Journal of Minerals, Metallurgy and Materials* **19**, 360–363 (2012).
26. Slavíček, J. *et al.* Wire-arc directed energy deposition of AZ61 magnesium alloy fabricated by cold metal transfer: Processing, microstructure, and mechanical properties. Preprint at <https://doi.org/10.5281/zenodo.15311035> (2025).
27. Arana, M., Ukar, E., Rodriguez, I., Iturrioz, A. & Alvarez, P. Strategies to reduce porosity in Al-Mg WAAM parts and their impact on mechanical properties. *Metals (Basel)* **11**, (2021).
28. Chen, R. *et al.* Effect of Al Content on the Microstructural and Grain Growth Kinetics of Magnesium Alloys. *Metals (Basel)* **12**, (2022).
29. Peng, L. *et al.* Al₈Mn₅ Particle Settling and Interactions with Oxide Films in Liquid AZ91 Magnesium Alloys. *Jom* **71**, 2235–2244 (2019).
30. Horynová, M., Zapletal, J., Doležal, P. & Gejdoš, P. Evaluation of fatigue life of AZ31 magnesium alloy fabricated by squeeze casting. *Mater Des* **45**, 253–264 (2013).
31. Mackie, D., Robson, J. D., Withers, P. J. & Turski, M. Characterisation and modelling of defect formation in direct-chill cast AZ80 alloy. *Mater Charact* **104**, 116–123 (2015).
32. Brancker, A. V. The use of CALCIUM STEARATE in wire drawing. *Scientific Lubrication* **1**, 17 (1949).